Facile and sustainable technique to produce low-cost high surface area mangosteen shell activated carbon for supercapacitors applications

V.N Kitenge[a,b], D.J Tarimo[b], K.O Oyedotun[b] G. Rutavi[b] and N. Manyala*[b]

[a]Department of Chemical Engineering, University of Pretoria, Pretoria 0028, South Africa.

[b]Department of Physics, Institute of Applied Materials, SARChI Chair in Carbon Technology and Materials, University of Pretoria, Pretoria 0002, South Africa.

*Corresponding authors' email: ncholu.manyala@up.ac.za

Highlights

- Mangosteen shell (MS-AC) was successfully converted into activated carbon.
- MS-AC was synthesized via a novel one-step carbonization/activation process.
- The optimal K_2CO_3 to MS-AC ratio (1:1) presented the highest specific capacitance.
- M-S AC was used as a positive/negative electrode in the symmetric supercapacitor.
- The assembled supercapacitor proves great potential in EmiFSI electrolyte.

Abstract

In this study, we have reported the effect of different activating agents, temperatures, and impregnation ratios on the porosity of mangosteen shell-derived activated carbons (M-S AC). The sample's characterization comprised of scanning electron microscopy (SEM), X-ray diffraction (XRD), Raman spectroscopy, and N_2 physisorption analysis. The M-S AC synthesized with K_2CO_3 as the activating agent displayed a high specific surface area of 2802.6 $m^2 g^{-1}$ and a flower-like morphology. Electrochemical measurements of the M-S AC synthesized with K_2CO_3 revealed a specific capacitance of 298.13 F g^{-1} at 0.5 A g^{-1} in a potential window of -0.9 – 0.0 V vs Ag/AgCl using 2.5 M KNO_3 electrolyte in a three-electrode measurement. An initial symmetric supercapacitor assembled with the optimized M-S AC as electrode material and 2.5 M KNO_3 as the electrolyte delivered a specific energy of 11.5 Wh kg^{-1} corresponding to a specific power of 0.4 kW kg^{-1} at 0.5 Ag^{-1} in a potential window of 1.6 V. A second assembled symmetric device using the same M-S AC as electrode material and 1-

Ethyl-3-methylimidazolium-bis(fluoroSulfonyl)imide (EmiFSI) ionic liquid as the electrolyte demonstrated high specific energy of 28.03 Wh kg^{-1} corresponding to a specific power of 0.7 kW kg^{-1} at 0.5 Ag^{-1} in a wider potential window of 2.8 V.

Graphical abstract

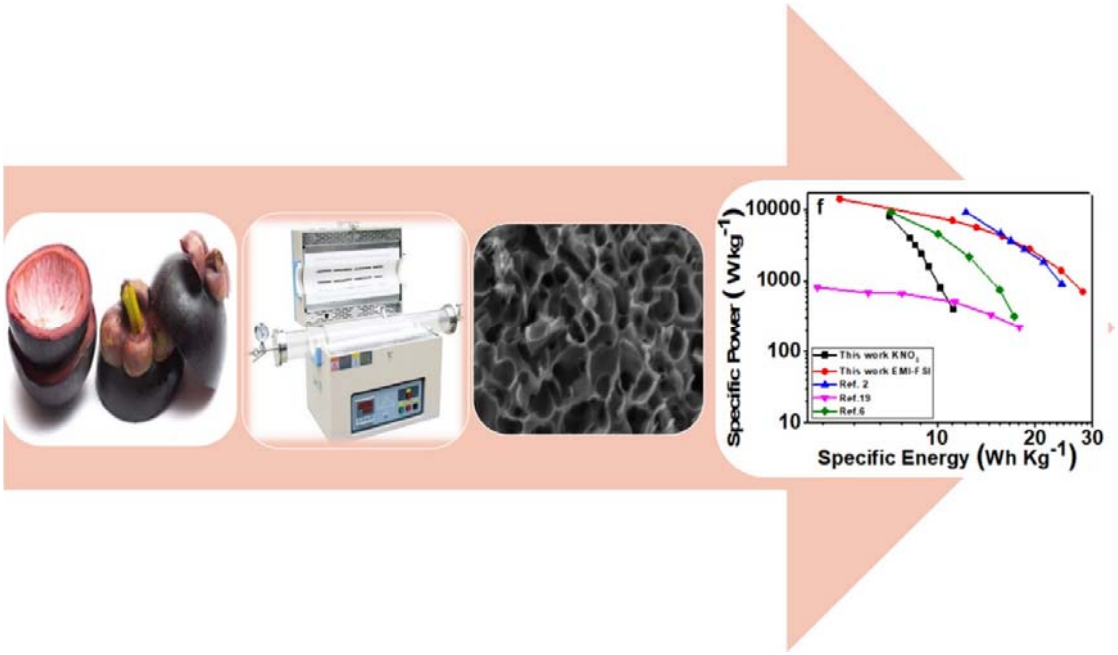

Keywords: Mangosteen; Biomass; Activated carbon; Ionic liquid; Specific energy; Supercapacitor.

1. Introduction

The twenty-first century has witnessed several climate change concerns as well as a significant drive toward sustainable global practices. Despite being environmentally friendly, renewable energy sources such as solar, wind, and wave are inadequate for continuous energy supply on their own [1-4]. A combination of energy storage technology and renewable energy resolves the challenge of a continuous energy supply as the energy storage will suppress the intermittent supply problems by discharging the accumulated energy and effectively filling the gap of

renewable energy-limited supply [5, 6]. Supercapacitors (SC) are prospective energy storage devices that attracted a lot of interest due to their highly reversible energy storage mechanism [1]. These devices have drawn interest in applications such as electric automobiles, micro-devices, and portable electronic devices, among others [7].

Supercapacitors store energy via electrochemical processes having different mechanisms and directly impacting their relative specific power and energy [8]. These storage mechanisms can be categorized into electrochemical double-layer capacitors (EDLCs) and pseudo-capacitors [9, 10]. In pseudo-capacitors, charges are stored via Faradaic redox reaction at the electrode/electrolyte interface while in EDLCs, charges are stored via fast electrostatic adsorption of the electrolyte ion on the surface of the electrode forming electric double layers at the same interface**.** Electrodes and electrolytes are two key parameters that affect the performances of supercapacitors. One strategy to advance SC's performance is to develop novel electrode materials while extending an understanding of nanoscale interfaces for electrochemical properties[1]. This will improve the specific energy of the device while benefitting from its distinctive high specific power.

EDLCs are usually made from materials having hierarchical pore size distribution (micropores, mesopores, and macropores), good electrical conductivity, and high specific surface area [11]. These properties are mainly found in carbon-based materials such as graphene, activated carbon (AC), carbon aerogels, and carbon nanotubes [12]. Due to its massive specific surface area and pore volume, activated carbon is a suitable novel generation of electrode materials for supercapacitors [13-15]. Additionally, activated carbon has a good adsorption capacity, chemical stability, well-ordered porous structures, and a cheap cost of production [16, 17]. The material can be efficiently synthesized from biomass which has the advantages of being freely available, renewable, easy to handle, and eco-friendly [18]. Its synthesis mostly involves pyrolysis followed by activation methods at elevated temperatures under inert gas. The

chemical diversity aspect of biomasses can also be explored to develop materials with capacitive properties valuable for supercapacitor applications [3].

Other studies on activated carbon synthesized from plant-based revealed the potential of activated carbon heteroatom doping and composites toward enhancing the material's electrochemical performance [4, 19, 20]. These multi-component carbon materials facilitate the design of adjustable pore size distributions as well as structures enabling fast electrolyte ions transport [19]. Ionic liquids (ILs) are innovative class of electrolytes in energy storage devices, particularly supercapacitors (ECs) [7]. Owing to their high potential windows, ILs enable high operational voltage which enhances the specific energy. 1-ethyl-3-methylimidazolium $[EMIm]^+$ and 1- butyl-3-methylimidazolium $[BMIm]^+$ are the mostly used ILs cations and can be merged with fluorinated anions including: bis (fluorosulfonyl)imide [FSI]- and bis(trifluoromethanesulfonyl)imide [TFSI]-. The selection of suitable electrolytes in SCs is highly dependent on the porosity of the material which should be compatible with the size of ILs ions.

Multiple plant-based biomass wastes were previously explored as precursors to produce activated carbon. Several parameters, responsible for enhancing electrochemical performances of activated carbon with precursors such as tree bark biomass [21], sugarcane bagasse [22], bamboo [23], banana peels [24], cassava peels [25], Orange peels [26], capsicum seed [27], coconut shells [28], peanut shell [5] and amarula seed husk [29], were previously reported. Mangosteen (Garcinia mangostana Linn) is popular for its pleasant taste and its usefulness as an ingredient for disease treatment medications [30]. The fruit originated in Malaysia and spread to the Philippines, Burma, India, and other regions of the world [31]. Copious amounts of mangosteen shell waste are generated without being recycled. Despite some reports on activated carbon from mangosteen shells [10, 16, 31, 32], the limited surface area and the production cost remain challenging. Studies on activated carbon production should aim to

develop facile and sustaining procedures to favour thoughts on upscaling the activated carbon production using biomass precursors.

This study focuses on a novel synthesis route to produce hierarchical activated carbon from waste mangosteen shells via a one-step carbonization/activation process. Its uniqueness consists of the integration of an intermediate ball milling of the activating agents and the precursor to obtain particles of the same size toward improving their contact during the synthesis. The study considered three activating agents (AA) namely KOH (strong alkaline), K_2CO_3 (middle alkaline), and H_3PO_4 (acidic). Afterward, variation of temperatures and impregnation ratios were explored with K_2CO_3 as it was the most promising activating agent after the preliminary synthesis. The morphology, structure, surface area, and electrochemical performances of the as-synthesized materials were also investigated. The results obtained demonstrated superior electrochemical performances with high specific energy and power densities highlighting the advantages of using ionic liquid as the electrolyte and the high quality of the porous carbon obtained with mangosteen shell waste precursors via the one-step merged carbonization/activation process.

2. Experimental method

2.1 Synthesis of the materials

Mangosteen fruits were purchased from a market in zando, a market in Kinshasa (D.R. Congo). The activated carbon was synthesized from the fruit shells (M-S) via a one-step merged carbonization/activation process. Before the synthesis, the M-S was thoroughly washed with deionized water and a slight volume of ethanol which was then placed in an oven to dry for 12 h at 60˚C. Afterward, the dried M-S powder was crushed into a fine powder using a vibrating ball mill at a power of 260 Watts for 15 min. Then, three quantities of 5 g of M-S were mixed with 5 g of H_3PO_4, K_2CO_3, and KOH, making a mass loading ratio of 1 AA to 1 M-S powder.

5 ml of deionized water was added to the mixtures to form cakes. The cakes were placed in an oven to dry for 12 h at 60˚C. The dried and compact block mixtures (cakes) were transferred one after another into a horizontal tube furnace set at 700 °C (ramp rate of 5 °C min^{-1}) for a period of 2 h while flowing argon gas at a rate of 200 sccm. The obtained products were soaked in hydrochloric acid (3 M) for 5 hours to get rid of unreacted salt/metals. The product was filtered, rinsed up to neutral pH, and dried for 12 h at 60˚C. The same procedure was used to synthesize the activated carbon when varying the mass loading ratio and temperatures for K_2CO_3 as the activating agent. Mass loading ratios of 1-0.5,1:1 and 1-2 were used for K_2CO_3. Temperatures of 600 °C, 700 °C, and 800 °C were used with the 1:1 M-S AC to K_2CO_3 mass ratios.

2.2 Characterization of the prepared materials

The textural properties of the as-synthesized materials were evaluated using A NOVA-touch LX^2 Quanta chrome surface area and pore size distribution (PSD) analyzer (NOVA touch NT 2 LX-1, 220 V, USA). The instrument used the BET method to measure the specific surface area from the adsorption/desorption isotherms with the relative pressure (P/Po) in the range of 0.05 to 0.95. The Density Functional Theory (DFT) method was utilized to determine the PSD. SEM morphological descriptions of the samples were obtained using a Zeiss Ultra Plus 55 field emission scanning electron microscope (FE-SEM, Akishima-shi, Japan) powered at 2.0 kV. The TEM images were obtained using an HR-TEM FEI Tecnai-F30 (Akishima-shi, Japan) instrument powered at 1.0 kV. To identify the synthesized materials phase structure, a theta/2theta geometry X-PERT PRO diffractometer XRD (PANalytical BV, Netherlands), with a cobalt source tube of wavelength (λ) of 0.154056 nm at 50 kV and 30 mA was utilized. The Raman analysis of the samples was performed with a WITec confocal Raman microscope

(WITec alpha 300 RAS+, Ulm, Germany) using 523 nm as laser wavelength, 4 mW as laser power, and 120 s spectral acquisition time.

2.3 Electrochemical characterization of the prepared material

The electrodes were prepared by mixing the active material (80 wt. %) with polyvinylidene difluoride (10 wt. %) and conductive carbon acetylene black (10 wt. %). The conductive carbon black was added to suppress the conductivity loss due to the PVDF (binder). N-methyl-2-pyrrolidone (NMP) was used as a solvent and added dropwise to the mixture. The mixture was then assorted evenly to make a slurry which was pasted on the surface of a 1×1 cm^2 cleaned Ni-foam used as the current collector. The electrodes were then dried in an electric furnace for 12 h at 60 °C. A Biologic VMP300 potentiostat (Knoxville TN 37,930, USA) utilizing the EC-Lab ® V11.33 software was used to perform the three-electrode and two-electrode measurements. The three-electrode measurement included glassy carbon as the counter electrode, Ag/AgCl as the reference electrode, and the electrode with the pasted synthesized material as the working electrode. The measurements were performed in 2.5 M KNO_3 electrolyte at room temperature. EmiFSI (Solvionic, 99.9%) ionic liquid was also used as an electrolyte in a three-electrode configuration using a T-cell with the electrode pasted with the synthesized material as the working electrode, a silver (Ag) disc as the reference, and a glassy carbon disc as the counter electrode. All the components were separated by filter paper. The T-cell was assembled in a glovebox (Inert Technologies, USA, O_2 & H_2O levels <1.0 ppm). The mass of the active materials varied between 2.5 – 3 mg cm^{-2} for all the materials in this study. The electrode cyclic voltammetry (CV) measurement in the three-electrode set-up was performed at several scan rates in a working potential ranging from -0.9 to 0.0 V vs Ag/AgCl for the negative electrode and 0.0 to 0.7 V vs Ag/AgCl for the positive electrode in 2.5 M KNO_3 electrolyte. Using EmiFSI, cyclic voltammetry (CV) measurements were performed at several

scan rates in a working potential ranging from -1.8 to 0.0 V on the negative potential and 0.0 to 1 V on the positive potential against a silver (Ag) disc reference electrode. The galvanostatic charge-discharges (GCD) were evaluated at various specific currents at the identical CV potential range for both positive and negative potentials. The electrochemical impedance of the samples were evaluated at open circuit potential with the frequencies varying from 10 mHz to 100 kHz.

2.3.1 Calculations

The half-cell's specific capacitance (C_{sp}) was determined with equations [24]:

$$C_{sp} = \frac{I\,\Delta t}{\Delta V\, m} \tag{1}$$

where m is the mass of the electrode; I is the applied current, Δt is the discharge time, and ΔV is the potential window.

The symmetric device masses balance was determined as follows [7]:

$$C_{sp,+}\, m_+\, \Delta V_+ = C_{sp,-}\, m_-\, \Delta V_- \tag{2}$$

where m_+ and m_- are the masses of the positive and negative electrodes; $C_{sp,+}$and $C_{sp,-}$ are the positive and negative electrode's capacitances; and ΔV_+ and ΔV_- are the potential window of the positive and negative electrodes, respectively.

The single electrode's specific capacitance (C_{single}) for the symmetric device was determined as follows:

$$C_{single} = \frac{4\,I\,\Delta t}{\Delta V\, M} \tag{3}$$

where M is the total mass of the two electrodes; I is the applied current, Δt is the discharge time, and ΔV is the voltage of the device.

To determine the device's specific energies (E_s) in joules per gram ($Wh\,kg^{-1}$) and their specific powers (P_s), equations (2a), (2b), and (3) were used:

$$E_s = \frac{1}{2}\, C_{single}(\Delta V)^2 = \frac{1000\ x\ C_{sp}\ x\ (\Delta V)^2}{2\ x\ 4\ x\ 3600} \tag{4a}$$

Where, C_{sp} is the device capacitance and ΔV is the cell's voltage.

Therefore,

$$E_s = \frac{C_{single}\Delta V^2}{28.8}(wh\ kg^{-1}) \tag{4b}$$

$$P_s = \ 3600x\frac{E_d}{\Delta t}(w\ kg^{-1}) \tag{5}$$

where, Δt is the device's discharge time.

The coulombic efficiencies were determined from the GCD curves via equations (4)

$$\epsilon = \frac{\Delta t\ discharge}{\Delta t\ charge}\ x\ 100\% \tag{6}$$

The activated carbon yield percentage was calculated as follows:

$$Yield\ \% = \frac{activated\ carbon\ (g)}{Mangosteen\ shell\ powder\ (g)} x100 \tag{7}$$

3. Results and discussions

Figure 1 illustrates the developed facile, and sustainable carbonization/activation method used to produce the activated carbon. This method consists of a pyrolysis combining the carbonization and the activation process. As compared to previous productions of mangosteen shells-activated carbon [10, 31-33], the method did not require prior pre-carbonization to obtain a hierarchical and highly porous activated carbon. This is, therefore, advantageous as it promotes a sustainable technology by reducing the activated carbon production steps. The

percentages of yield of carbon obtained using KOH, K_2CO_3, and H_3PO_4 were 30.5%, 39.6 %, and 26.2%, respectively. It is suggested that the presence of K_2CO_3 within the core of the precursor restricted the formation of tar and additional liquids such as methanol and acetic acid by forming cross-links, and obstructing the shrinkage of the precursor particle by occupying substantial volumes [34]. This supports previous findings suggesting that K_2CO_3 only reacts with the char and gets removed during the gasification process. Consequently, the process occurs in an inert atmosphere as follows [35]:

$$K_2CO_3 + 2C \rightarrow 2K + 3CO \quad (8)$$

$$K_2CO_3 \rightarrow K_2O + CO_2 \quad (9)$$

The activation process using KOH is likely to occur as follows [36]:

$$6KOH + 2C \rightarrow 2K + 3H_2 + 2K_2CO_3 \quad (10)$$

The ones involving H_3PO_4 may have occurred as follows [37]:

$$nH_3PO_4 \rightarrow H_{n+2}P_nO_{3n+1} + (n-1)H_2O \quad (11)$$

$$H_{n+2}P_nO_{3n+1} \rightarrow P_4O_{10} + H_2O \quad (12)$$

$$P_4O_{10} + C \rightarrow P_4O_6 + CO_2 \quad (13)$$

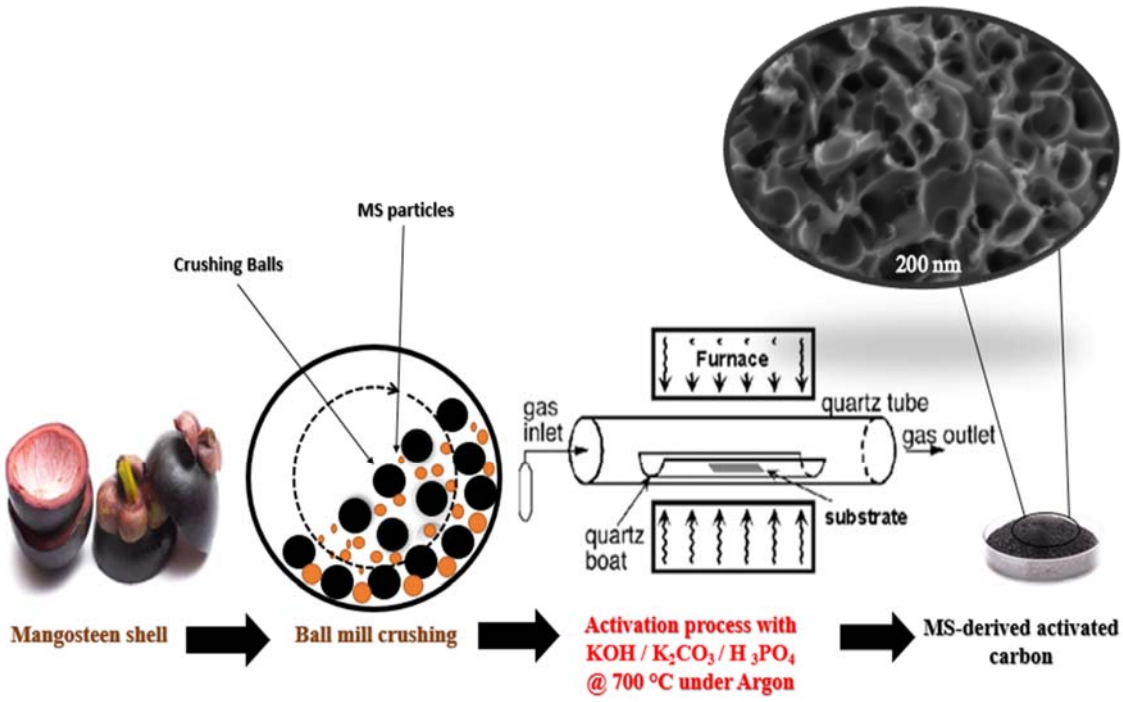

Figure 1: Synthesis route of waste mangosteen shell-derived activated carbon.

3.1 N_2-adsorption/desorption analysis, Scanning electron microscopy, X-ray diffraction, and Raman analysis

The synthesis optimization involved different activating agents to identify the ideal MS-AA combination that will yield activated carbon having the most promising textural properties. N_2-adsorption/desorption analysis was performed to obtain the samples' textural properties. Their specific surface areas evaluated through Brunauer-Emmett-Teller (BET) measurement are displayed in figure 2. Figure 2(a) illustrates the materials' isotherms for the M-S activated carbon (M-S AC) synthesized with different activating agents (KOH, K_2CO_3, and H_3PO_4) as well as the M-S AC synthesized with different K_2CO_3 impregnation ratios (1:0.5, 1:1, and 1:2). All the as-synthesized materials displayed a type-I isotherm with H4 hysteresis loop. Generally, type-I isotherms are uniquely observed for the adsorption of gases on microporous materials whose adsorbent surfaces are covered by monolayers of the adsorbent molecules [38]. H4

hysteresis loops indicate the presence of slit-shaped pores suggesting the presence of micropores and mesopores. The high SSA and the volume adsorbed of 1:1 K_2CO_3 to M-S AC shows the greater percentage of micropores and mesopores compared to other synthesized M-S AC. The synergistic combination of pore production, pore expansion, pore combination, and pore collapse results in the development of AC's porous structure. Pores are formed via a gasification reaction caused by alkali metal when using alkaline activating agents such as KOH, and K_2CO_3 occurs [39]. The role of metallic potassium vapor is unique and key for the development of pores, and such a role is not present in the pyrolysis by acidic activating agents such as H_3PO_4. In this case, it enabled K_2CO_3 to be reduced by carbon to form K, K_2O, CO, and CO_2 so that more pores could be formed. This explains why the 1:1 H_3PO_4 to M-S AC has a lower specific surface area as compared to 1:1 K_2CO_3 to M-S AC and 1:1 KOH to M-S AC. Furthermore, it is suggested that a collective effect involving the precise temperature, activating agent, and impregnation ratio in the synthesis of 1:1 ratio of K_2CO_3 enhanced the textural properties of the material as compared to the 1:1 KOH to M-S AC synthesis. Also, the stoichiometric amount of K (alkali metal) in K_2CO_3 certainly played a role in the greater textural properties obtained with the 1:1 K_2CO_3 to M-S AC material during the gasification reaction in the synthesis. The observed structures in figure 2(a) can be related to figure 2(b) which displays the pore size distribution of the prepared samples.

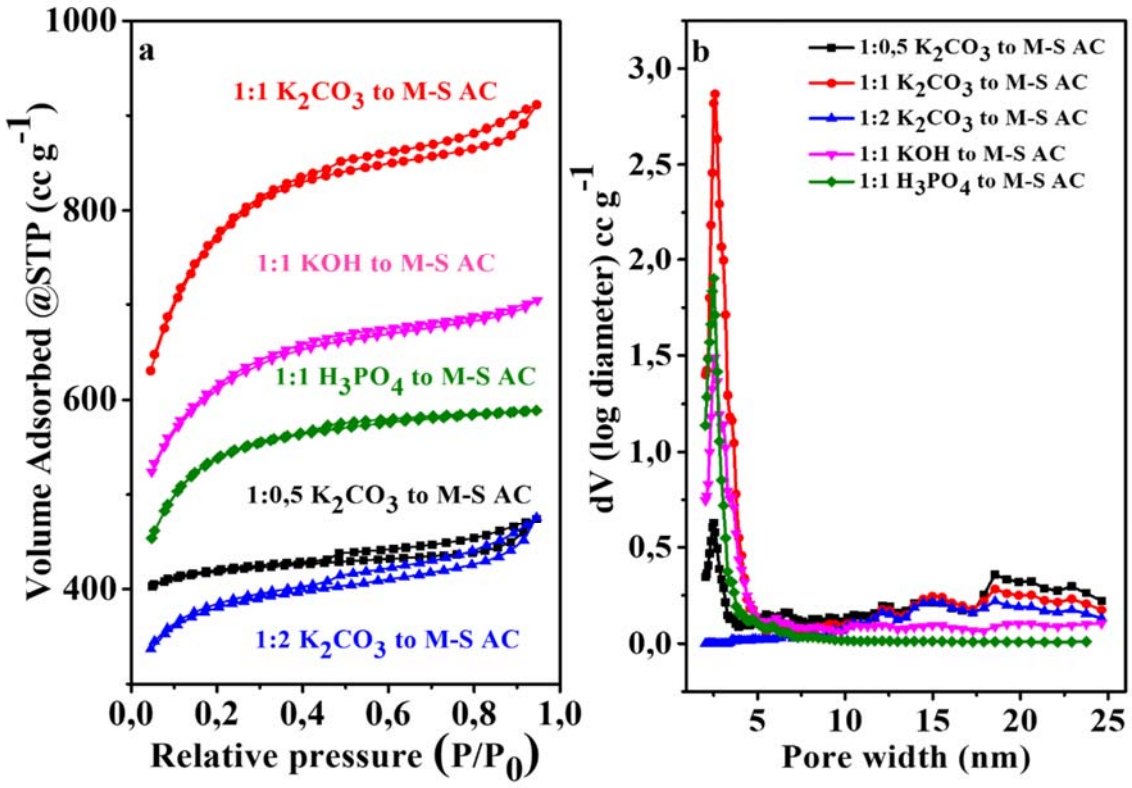

Figure 2: (a) N_2 adsorption-desorption isotherms and, (b) pore size distribution.

The reaction mechanisms for the porous structure formation can be seen in figure 3. The figure illustrates the interactions between MS and KOH (1), K_2CO_3 (2), and H_3PO_4 (3). It describes the pores sites created on the surface of the nanocarbon particles (the black circular shape) using different activating agents. An outstanding porous structure is obtained with the 1:1 K_2CO_3 to M-S AC and this is described by the higher amounts of pores (white stripes) present in the synthesis of this sample.

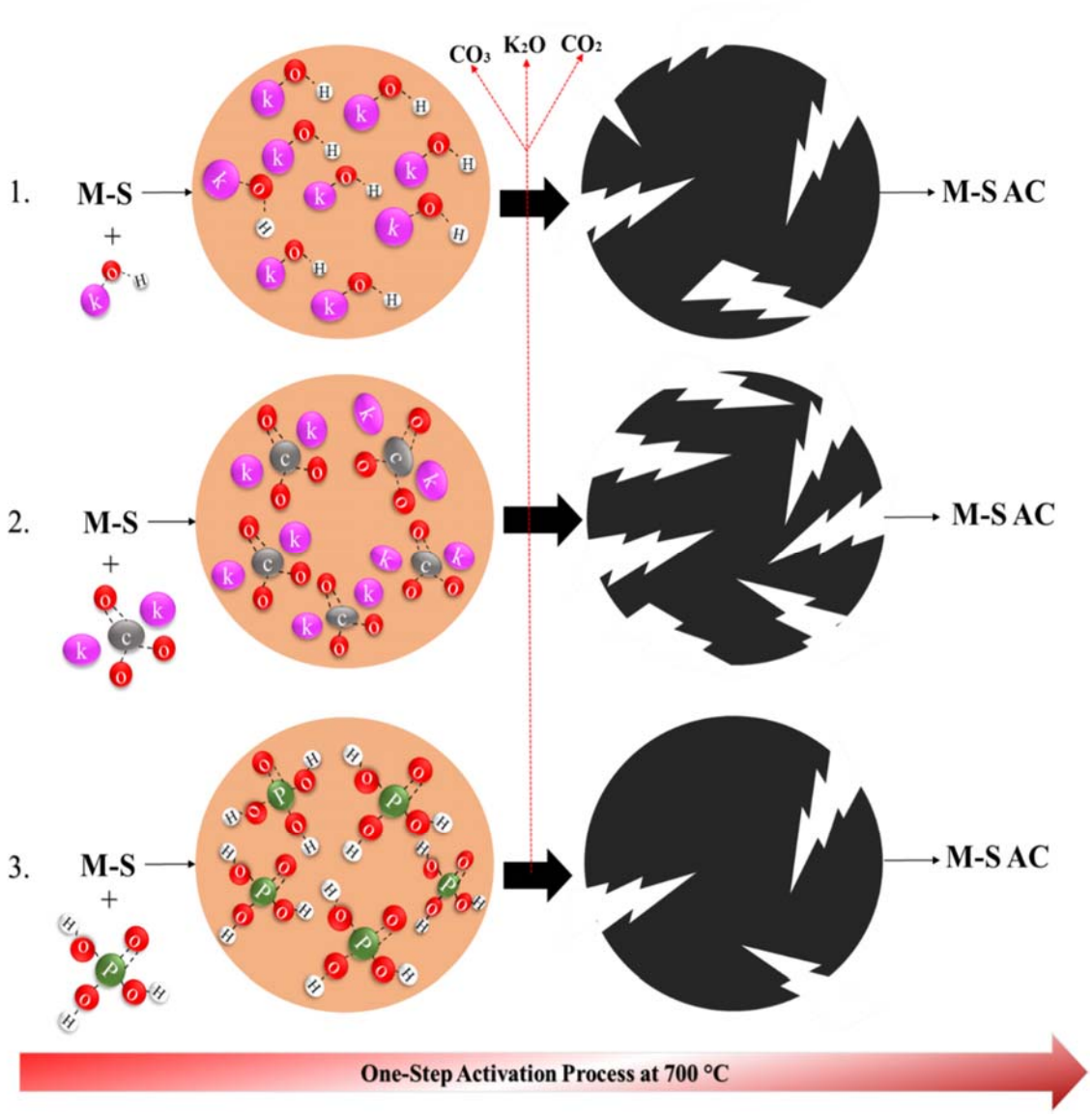

Figure 3: Reaction mechanism between MS and KOH (1), K_2CO_3 (2), and H_3PO_4 (3).

Table 1 provides a summary of the specific surface area ($m^2\ g^{-1}$), micro-pores volume (cc g^{-1}), total pores volume (cc g^{-1}), and average pore sizes (nm) whereby values of 2803 $m^2\ g^{-1}$, 0.9 cc g^{-1}, 1.1 cc g^{-1}, and 2.1 nm, respectively, were obtained with the 1:1 K_2CO_3 to M-S AC material. The 1:1 K_2CO_3 to M-S AC activated carbon proved superior textural properties compared to when the impregnation ratio was lowered to 1:0.5 M-S to K_2CO_3 or increased to 1:2 M-S to

K_2CO_3, indicating the optimum impregnation ratio. The sample's specific surface area also demonstrated a higher value as compared to the values obtained by Yang et. al [10]: 2623 m^2 g^{-1}, Zhang et. al [32]: 1700 m^2 g^{-1}, Li et. al [40]: 1270 m^2 g^{-1}, Chen et. al [31]: 1123 m^2 g^{-1} and Iradukunda et. al [41]: 1079 m^2 g^{-1} when using mangosteen shell as a precursor. The obtained results showed that the M-S AC synthesis route involving the 1:1 K_2CO_3 impregnation ratio is a potential way of improving the specific surface area of the carbon material.

Table 1: The textual properties of the as-synthesized samples.

AA to MS ratio	1:0,5 K_2CO_3	1:1 K_2CO_3	1:2 K_2CO_3	1:1 KOH	1:1 H_3PO_4
Surface area (m^2/g)	1453	2803	1435	2248	2013
Micropore volume (cc/g)	0.6	0.9	0.5	0.8	0.7
Total pore volume(cc/g)	0.7	1.4	0.7	1	0.9
Average Pore Size (nm)	2	2.1	2	1.9	1.8

Several other plant-based biomass wastes were previously considered precursors to produce activated carbon. Table 2 summarizes some plant-based wastes, their synthesis methods as well as the specific surface area obtained after the synthesis.

Table 2: Some plant-based derived activated carbon synthesis methods and specific surface areas

Precursor	Pre-carbonization/ Pre-treatment	Synthesis method	Specific surface area ($m^2 g^{-1}$)	Ref.
Tree bark biomass	Yes	Synthesized directly by a KOH activation process followed by carbonization	1018	[21]
Sugarcane bagasse	Yes	Two-step method of carbonization and chemical activation	1058	[22]
Bamboo	No	Single-stage phosphoric acid (H_3PO_4) activation	1492	[23]
Banana peel	Yes	Hydrothermal followed by carbonization process	1362	[24]
Cassava peels	Yes	Pre-leaching cassava peels with NaOH followed by KOH activation and carbonization	1684	[25]
Orange peel	Yes	Carbonization followed by KOH activation process	2160	[26]
Capsicum seed	No	Single-step carbonization	2201	[27]
Coconut shell	Yes	Freezing pre-treatment followed by pyrolysis	2410	[28]
Peanut shell	Yes	Two-step pyrolysis technique at elevated temperatures.	2547	[5]
Mangosteen shell	Yes	Facile combined method of carbonization and NaOH treatment processes	2623	[10]
Amarula seed husk	Yes	Hydrothermal water salt followed by KOH activation	1672	[29]
Mangosteen shell waste	**No**	**One-step carbonization/activation process**	**2803**	**This work**

Despite not being pre-carbonized (pre-treated), the M-S AC synthesis involving the 1:1 K_2CO_3 impregnation ratio demonstrated a higher specific surface area as compared to the techniques

mentioned in table 2. This demonstrates the indubitable effectiveness of the developed technique. The intermediate ball milling induced the efficiency of the synthesis process by reducing the mangosteen shell waste into fine powder thus improving the contact with the crushed activating agent.

Since the 1:1 K_2CO_3 to M-S AC impregnation ratio displayed a superior textural property, the remaining investigation focused on detailing the samples obtained via M-S to K_2CO_3 impregnation ratios. Figure 4 (a_1 – c_1) and (a_2 – c_2) display the SEM images of the as-synthesized materials using various impregnation ratios at low and high magnifications. The images display clear connected cavities on the materials' surfaces which result from the interactions of the M-S with different K_2CO_3 impregnation ratios. Figure 4 (a_1-a_2) illustrates the as-synthesized material SEM images obtained with the 1:0.5 K_2CO_3 to M-S AC. The images display undefined morphology with inconsistent and unevenly distributed micro-cavities. Figure 4 (b_1-b_2) illustrates the 1:1 K_2CO_3 to M-S AC which reveals a highly mesoporous arrangement with much more open cavities and a flower-like morphology. Figure 4 (c_1-c_2) displays the 1:2 K_2CO_3 to M-S AC presenting a wrecked structure having a cracked micro-sized morphology. The cavities observed with the 1:2 K_2CO_3 to M-S AC appear dismantled due to an excessive amount of K_2CO_3. The uniform porous structure obtained in figure 4 (b_1-b_2) confirm the ideal impregnation ratio under the previously specified conditions is 1:1 M-S to K_2CO_3. It also demonstrates that porous carbon synthesis is directly affected by the amount of K_2CO_3. TEM images are illustrated in figure 4 (a_3-c_3). These images are reflections of morphologies obtained with the SEM with all samples illustrating cavities. A regular framework with interconnected cavities is obtained with the 1:1 M-S to K_2CO_3 in figure 4 (a_2) which confirms the mesoporous arrangement obtained with its SEM. The inconsistent and uneven distribution of micro-cavities obtained with 1:0.5 M-S to K_2CO_3 as well as the

cracked micro-sized features obtained with 1:2 M-S to K_2CO_3 on the SEM analysis can also be seen in the TEM images in figures a_1 and a_3, respectively.

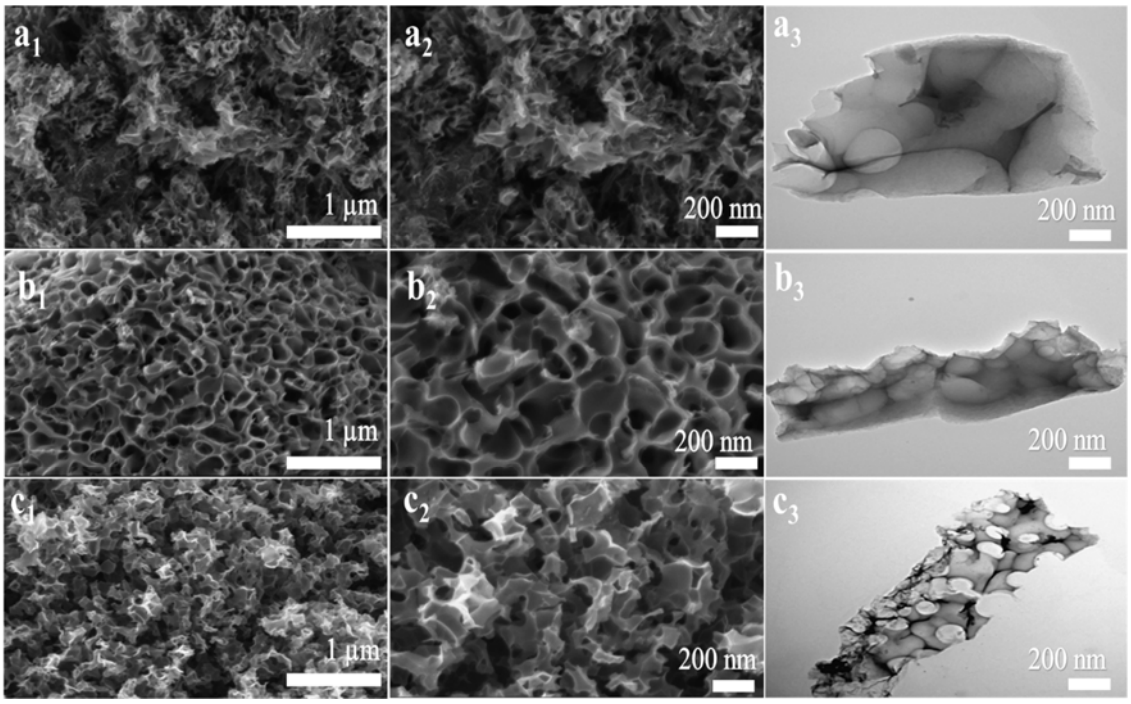

Figure 4: ($a_1 – c_1$) low magnification SEM images, ($a_2 – c_2$) high magnification SEM images & ($a_3 – c_3$) TEM images of 1:0.5 K_2CO_3 to M-S AC, 1:1 K_2CO_3 to M-S AC, and 1-2 K_2CO_3 to M-S AC, respectively.

Figure 5 (a) illustrates the EDS spectrum, as well as compositions of the K_2CO_3 to M-S AC, synthesized materials. All the spectra prove the high presence of carbon with lower O concentration, and a highest intensity pick was obtained for the 1:1 K_2CO_3 to M-S AC. The composition percentage of the materials also indicates a higher carbon percentage for the 1:1 K_2CO_3 to M-S AC. The elemental maps of the samples are illustrated in figure 5 (b). The images illustrate uniform distributions of carbon in the selected areas on all samples.

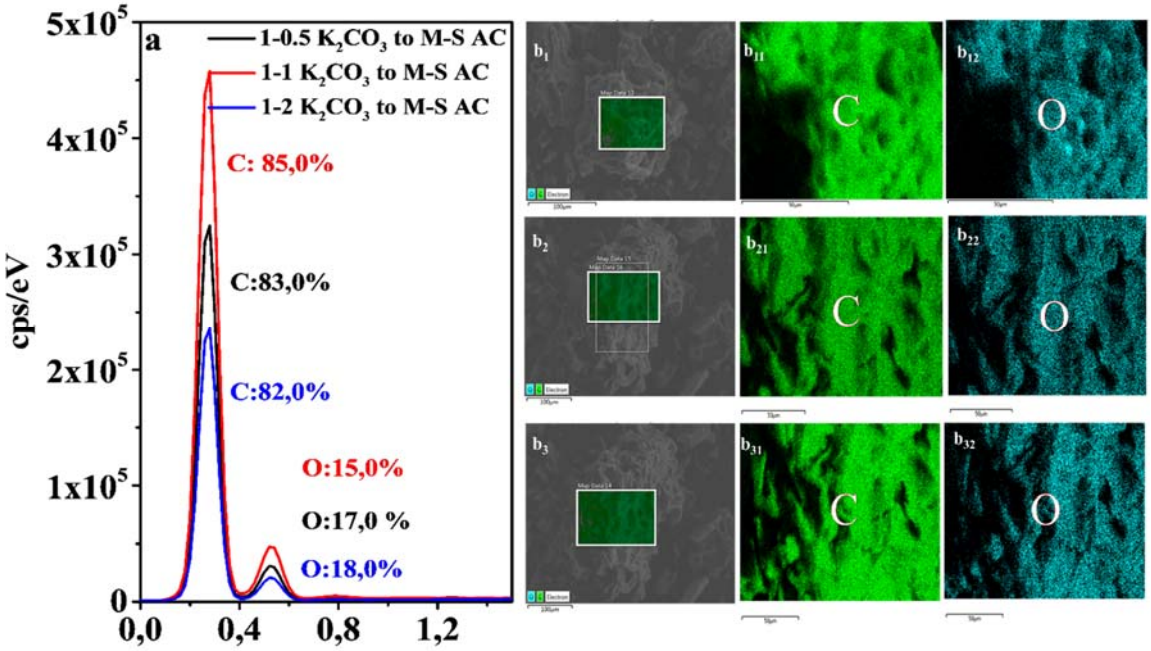

Figure 5: (a) EDS elemental composition and spectrum, and (b) carbon and oxygen mapping of 1:0.5 K_2CO_3 to M-S AC, 1:1 K_2CO_3 to M-S AC, and 1:2 K_2CO_3 to M-S AC samples.

Figure 6 illustrates the XRD and Raman analysis of the as-synthesized K_2CO_3 to M-S AC samples. The XRD patterns indicating the phase structure of the as-synthesized materials with different K_2CO_3 impregnation ratios are displayed in figure 6 (a). The figure illustrates the (002) and (101) planes of carbon at 2θ of 12.02° and 42.51°as per the JCPDS card No. 41–1487 for all the samples [10, 42, 43]. The XRD pattern width for the 1:2 K_2CO_3 to M-S AC appears prominently increased as compared to the one for 1:1 K_2CO_3 to M-S AC. The width increments illustrated with the 1:1 K_2CO_3 to M-S AC are attributed to the sample's widening and burn-off due to an excessive amount of activating agent. The patterns also demonstrate that high purity porous carbon was produced from the mangosteen shell waste as no intermediate planes of metal traces were observed related to the increase in amorphous degree despite the use of an activating agent with a metallic salt.

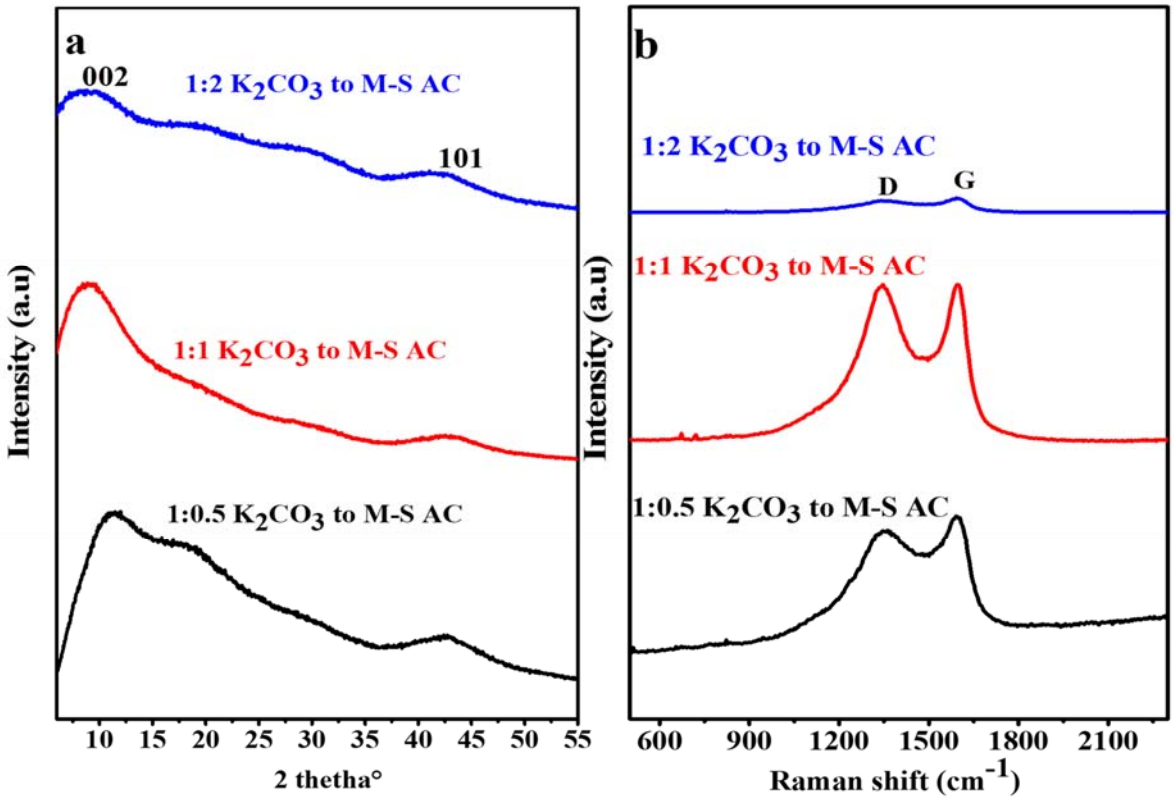

Figure 6: (a) XRD patterns, and (b) Raman spectrum of the as-synthesized samples, respectively.

Figure 6 (b) illustrates the spectra obtained for the Raman analysis of the materials. The figure illustrates D-bands at about 1349.7 cm^{-1} and the G-bands at about 1629.5 cm^{-1} exhibiting carbon materials' typical characteristic picks for all the samples [24]. The band intensities can be seen to increase as the K_2CO_3 impregnation ratio increased from 0.5 to 1. This indicates a lower degree of graphitization for the 1:1 K_2CO_3 to M-S AC carbon material. When increasing the K_2CO_3 ratio to 2, the G-band and the D-band intensities are seen to drastically decrease. The degree of defects in the material was evaluated by I_d/I_g ratio in which 0.94, 1, and 0.95 were obtained for 1:0.5 K_2CO_3 to M-S AC, 1:1 K_2CO_3 to M-S AC, and 1-2 K_2CO_3 to M-S AC, respectively. The 1:1 K_2CO_3 to M-S AC illustrated a low degree of graphitization revealing good interaction between K_2CO_3 and the precursors which agrees well with the gas adsorption

analysis[44]. Also, the XRD patterns obtained are corresponding well with the Raman analysis spectrum whereby 1:1 K_2CO_3 to M-S AC remains the optimal sample in this investigation.

3.2 Electrochemical evaluations

3.2.1: Three-electrode measurements

Figure S 1(a) and (b) illustrate the CV patterns as well as GCD patterns, respectively, of positive electrodes of the samples obtained with different activating agents. Figure S 1(c) and (d) display the CV and GCD patterns of the same samples when used as negative electrodes. Figure S 1(e) shows the EIS Nyquist plot, with the inset showing the high-frequency region for all samples. The overall analysis demonstrates electrochemical performance dominance of 1:1 K_2CO_3 to M-S AC with regards to 1:1 KOH to M-S AC and 1:1 H_3PO_4 to M-S AC. In terms of specific capacitance (C_{sp}), the 1:1 KOH to M-S AC and 1:1 H_3PO_4 to M-S AC samples presented closed values on the positive electrode (~91.07 F g^{-1}) as illustrated in figure S 1(b). However, the 1:1 M-S to K_2CO_3 carbon material illustrated a specific capacitance approximately 2 times superior then 1:1 KOH to M-S AC and 1:1 H_3PO_4 to M-S AC when used as negative electrodes.

Figure S 2(a) and (b) display the EIS Nyquist plot, with the inset showing the high-frequency region and the electrical series resistance (R) values for 1:1 K_2CO_3 to M-C AC samples at temperatures of 600, 700, and 800 °C, respectively. Figure S 2(a) illustrates a diffusion path closer to the y-axis for the sample synthesized at 700 °C. The electrical series resistance (R_s) values of the samples also proved to be lower for the 700 °C as compared to the samples synthesized at 600, and 800 °C. Additionally, the 700 °C sample displayed no semi-circles as compared to the other samples. The results prove the higher ionic conductivity obtained for the

1:1 K_2CO_3 to M-C AC material synthesized at 700 °C and underpin the selection of this temperature as optimal for the synthesis of the M-S derived activated carbon.

Figure 7 illustrates the electrochemical features (CV, GCD, and EIS) of the as-synthesized 1:0.5 K_2CO_3 to M-S AC, 1:1 K_2CO_3 to M-S AC, and 1:2 K_2CO_3 to M-S AC carbon materials in a three-electrode configuration. Figure 7 (a) displays the positive electrode CV patterns with a linear rectangular shape characteristic of the EDLC. Also, a pronounced shape, with a higher current response, is obtained with the 1:1 K_2CO_3 to M-S AC as compared to the other samples. Similarly, linear rectangles are demonstrated when the carbon materials are tested as a negative electrode in figure 7 (c). The 1:1 K_2CO_3 to M-S AC carbon material exhibited a superior current response and a broader quasi-rectangular shape as both positive and negative electrodes. The 1:1 K_2CO_3 to M-S AC's characteristic features including specific surface area appear to favour good electrical conductivity resulting from its highly porous structure. This property allows a larger number of ions to diffuse within the pores of the material's 3D interconnection framework. The obtained GCD patterns of the positive and negative K_2CO_3 to M-S AC electrodes are illustrated in figures 7 (b) and (d), respectively. The patterns illustrate a linear charge-discharge with a triangular shape demonstrating the typical capacitive nature of the samples. It can also be seen that the 1:1 K_2CO_3 to M-S AC demonstrates a longer discharge time as compared to the 1:0.5 K_2CO_3 to M-S AC and 1:2 K_2CO_3 to M-S AC in both figures. The specific capacitance (C_{sp}) at 0.5 A g^{-1} for the positive electrodes are 82.56, 91.5, and 58.02 F g^{-1} for the 1:0.5 K_2CO_3 to M-S AC, 1:1 K_2CO_3 to M-S AC, and 1:2 K_2CO_3 to M-S AC samples, respectively. On the negative electrode tests, the specific capacitance values obtained are 170.84, 298.13, and 122.49 F g^{-1} for the 1:0.5 K_2CO_3 to M-S AC, 1:1 K_2CO_3 to M-S AC, and 1:2 K_2CO_3 to M-S AC samples at 0.5 A g^{-1}, respectively. Both the positive and the negative electrodes for 1:1 K_2CO_3 to M-S AC demonstrate higher specific capacitance. The higher specific capacitance values obtained with the 1:1 K_2CO_3 to M-S AC suggest a higher charge

accumulation on the electrodes. The enhanced large mesoporous surface obtained also enabled the enhancement of the material capacitance and rate performance [2]. Studies in the literature indicate increment of specific capacitance as per cations size as $Li^+ < Na^+ < K^+$ [45]. The K^+ cation and NO_3^- anion within the selected 2.5 M KNO_3 contributed to a rapid ion transmission on the electrode/electrolyte interface due to their adequate ions size ideal for the porous structure of the 1:1 K_2CO_3 to M-S AC. The selected aqueous-based electrolyte (KNO_3) is also advantageous as its neutral pH renders it safe, non-corrosive, and non-flammable.

Figure 7(e) illustrates the EIS Nyquist plot, with the inset showing high-frequency regions for 1:0.5 K_2CO_3 to M-S AC, 1:1 K_2CO_3 to M-S AC, and 1:2 K_2CO_3 to M-S AC. The plot displays a pronounced semi-circle for the 1:0.5 K_2CO_3 to M-S AC and 1:2 K_2CO_3 to M-S AC. These semi-circles occur due to charge transfer resistance between these materials and the electrolyte [46]. The 1:1 M-S to K_2CO_3'outstanding ionic conductivity and low charge transfer resistance resulted in a non-existent semi-circle. This trend goes hand in hand with the different R_s values of 0.98, 0.57, and 1.31 Ω obtained for 1:0.5 K_2CO_3 to M-S AC, 1:1 K_2CO_3 to M-S AC, and 1:2 K_2CO_3 to M-S AC, respectively. The 1:1 K_2CO_3 to M-S AC low R value confirms its excellent conductivity and faster mass transport between the electrodes and the electrolyte obtained when used as electrode material. Additionally, the figure indicates shorter and near the ideal vertical line diffusion path length for the 1:1 K_2CO_3 to M-S AC. These electrochemical impedance spectrometry features confirm that the 1:1 M-S to K_2CO_3 synthesized carbon material is the most electrochemically conductive material in this investigation.

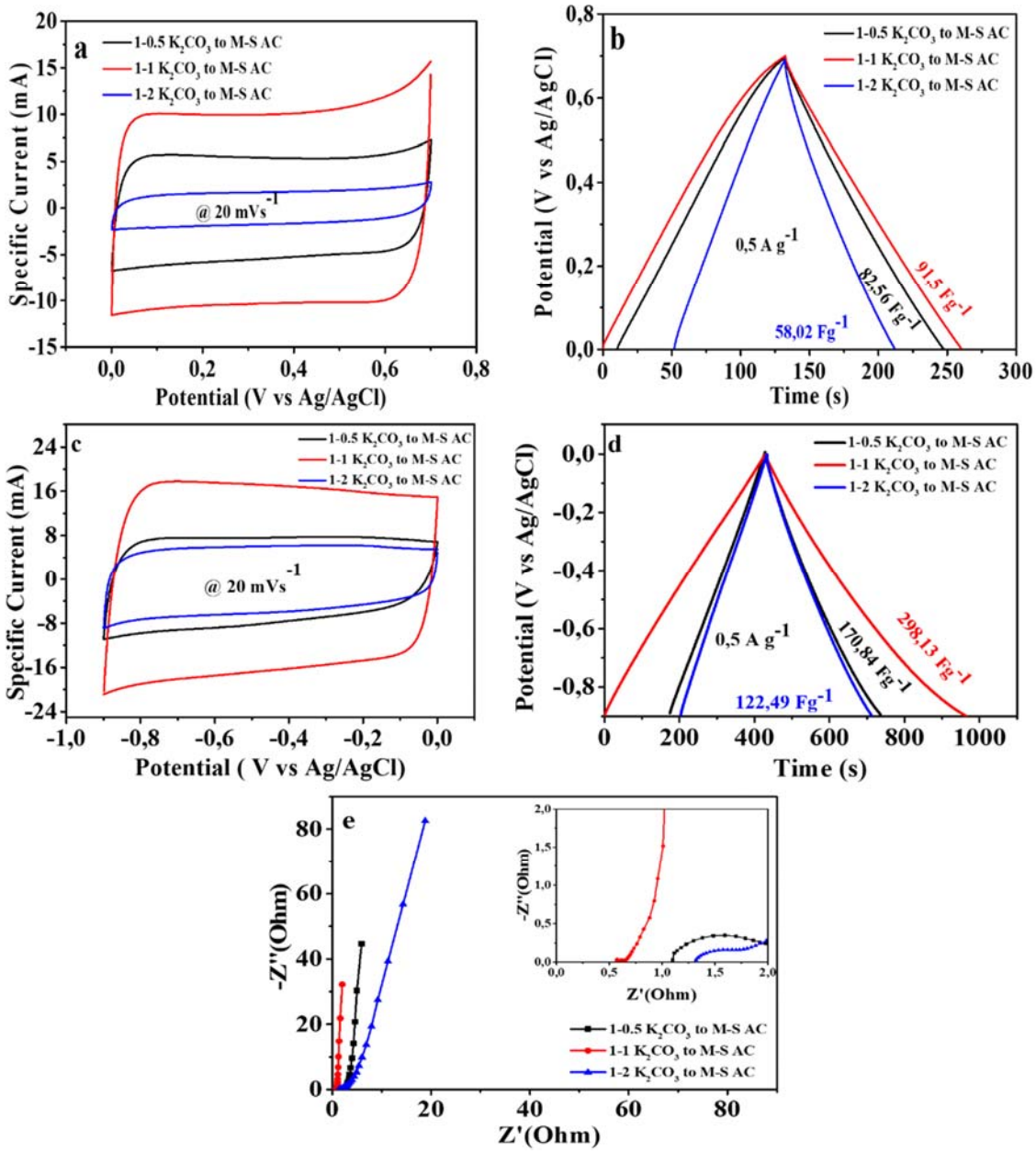

Figure 7: (a, c) Positive and negative electrode CV patterns at 20 mV s^{-1}, (b, d) positive and negative electrode GCD patterns at 0.5 A g^{-1}, and (e) EIS Nyquist plot, with the inset to the figure showing low-frequency region for samples with different K_2CO_3 ratio.

The outstanding electrochemical properties demonstrated by 1:1 M-S to K_2CO_3 synthesized carbon material inspired further detailed electrochemical measurements illustrated in figure 8.

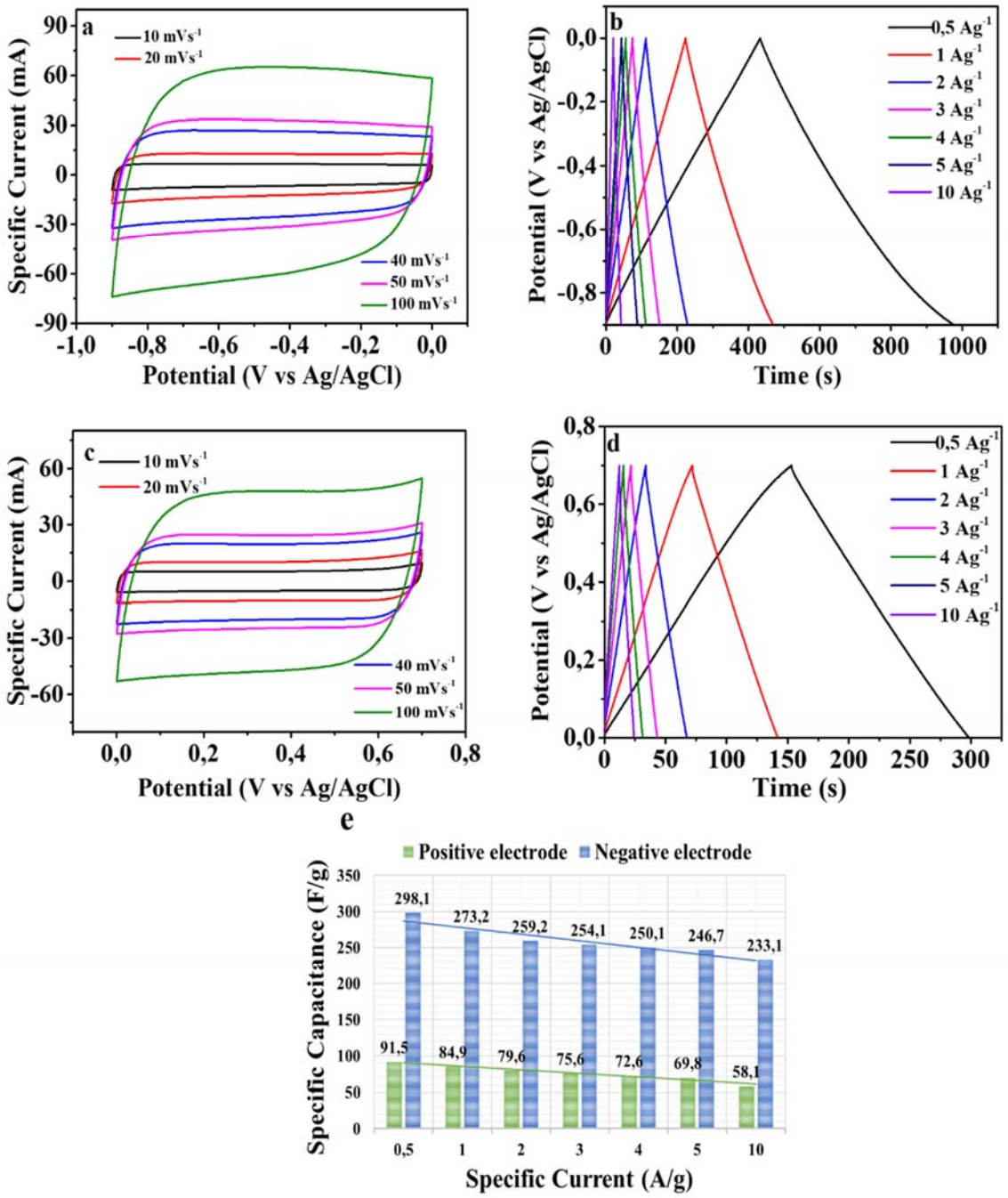

Figure 8: (a, and c) Positive and negative electrode CV curves at various scan rates, (b, and d) positive and negative electrode GCD curves at distinct specific currents, and (e) specific capacitance versus specific current for 1:1 K_2CO_3 to M-S AC.

Despite the different scan rates, Figures 8 (a) and (c) still illustrate rectangular CV curve shapes for both the positive and negative electrodes. However, the CV curves show the existence of redox peaks in the positive potential range (figure 8 (c)), which is attributed to the continuing electrochemical redox reactions caused by the abundance of oxygen functional groups, generally having strong redox reactivity characteristics in the positive potential [47]. Figures 8 (b) and (d) display characteristic EDLC behaviours with triangular charge-discharge curves even at higher specific currents. The optimized carbon material displays sustaining capacitance retention as displayed in figure 8 (e). The material was able to preserve 78.2 % and 63.5 % of its initial capacitance when the specific current was increased to 10 A g^{-1} for the negative and positive electrodes, respectively. These results exhibit the potential of the material as both positive and negative electrodes for electrical double-layer capacitor devices.

3.2.2 Two-electrode system measurement

A M-S AC//M-S AC symmetric device using 1:1 K_2CO_3 to M-S AC as both negative and positive electrode material was initially assembled using 2.5 M KNO_3 as the electrolyte. The operative areal masses of the materials on the device's electrodes, determined based on equation (3) were approximately 3.2 mg cm^{-2}, for the negative electrode and 4.1 mg cm^{-2} on the positive electrode making an overall device total mass equivalent to 7.3 mg cm^{-2}, with the electrode thickness of about 96 µm measured with a micrometer. A standard 2032 grade coin cell was used for the casing, and the electrodes were separated using filter paper.

Figure 9 (a) displays the CV patterns of the symmetric device at various scan rates in an overall potential window of 1.6 V. This potential window was expected as it reflects the steady addition of the potential window obtained on the negative and positive electrode tests. The constant linear rectangular shape of the CV at several scan rates indicates that the manufactured device is an electrical double layer capacitor as expected. It also demonstrates a negligible decay of

the capacitance at higher scan rates indicating an outstanding rate capability [48]. The device GCD curves at multiple specific currents are triangular as displayed in figure 9 (b). This behaviour corresponds with the EDLCs particularities observed in figure 9 (a) and approves the fast ions transfer process occurring in the device charge-discharge process. The specific capacitance at various specific currents for this device is summarized in figure 9 (c). The device exhibited a sustaining specific capacitance of 125.9 F g^{-1} at 0.5 A g^{-1}. At 10 A g^{-1}, the device still demonstrates a capacitance of 80.3 F g^{-1} and retains 63.7% of its initial capacitance. A cycling capability test was performed with constant charge-discharge at 20 A g^{-1} for 50000 cycles as displayed in figure 9 (d). After the pre-set cycles the device displays coulombic efficiency of 99.9 % and exceptional capacitance retention of 99.6%. The observed resistive character of the GCD profiles at around the initial 5000 cycles as shown in figure 9 (d), suggests some difficulties in charge propagation, leading to the high drop of capacitance which is then recovered at about 13000 cycles. The inset SEM to figure 9 (d) of the material after cycling still illustrates an ordered porous structure as compared to the initial images before this analysis illustrated in figures b_1-b_2. Figure 9 (e) illustrates the fitting of the Nyquist plot data with the equivalent circuit (inset to the figure) of the device. This result was obtained using a fitting program that uses the complex non-linear least square method for circuit elements. The obtained circuit's component can change based on the device evaluated. The circuit involved a resistor (R_{st}) related to the resistance located at the interface between the electrode and the 2.5 M KNO_3 electrolyte. The charge transfer resistance (R_{CT}) component presented in the circuit corresponds to the adsorption process occurring within the device due to the electrolyte ion's dimensions. The circuit also comprise mass capacitances (Q) due to the imperfect capacitive behaviours located in the low frequency region. Finally, the circuit comprised a capacitor (C_{DL}) which indicates the double layer capacitance occurring in the device. The plot

(which predicts the diffusion kinetics at the electrode's surface) indicates a non-pronounced semi-circle in the high-frequency region with an R_s value of 0.56 Ω.

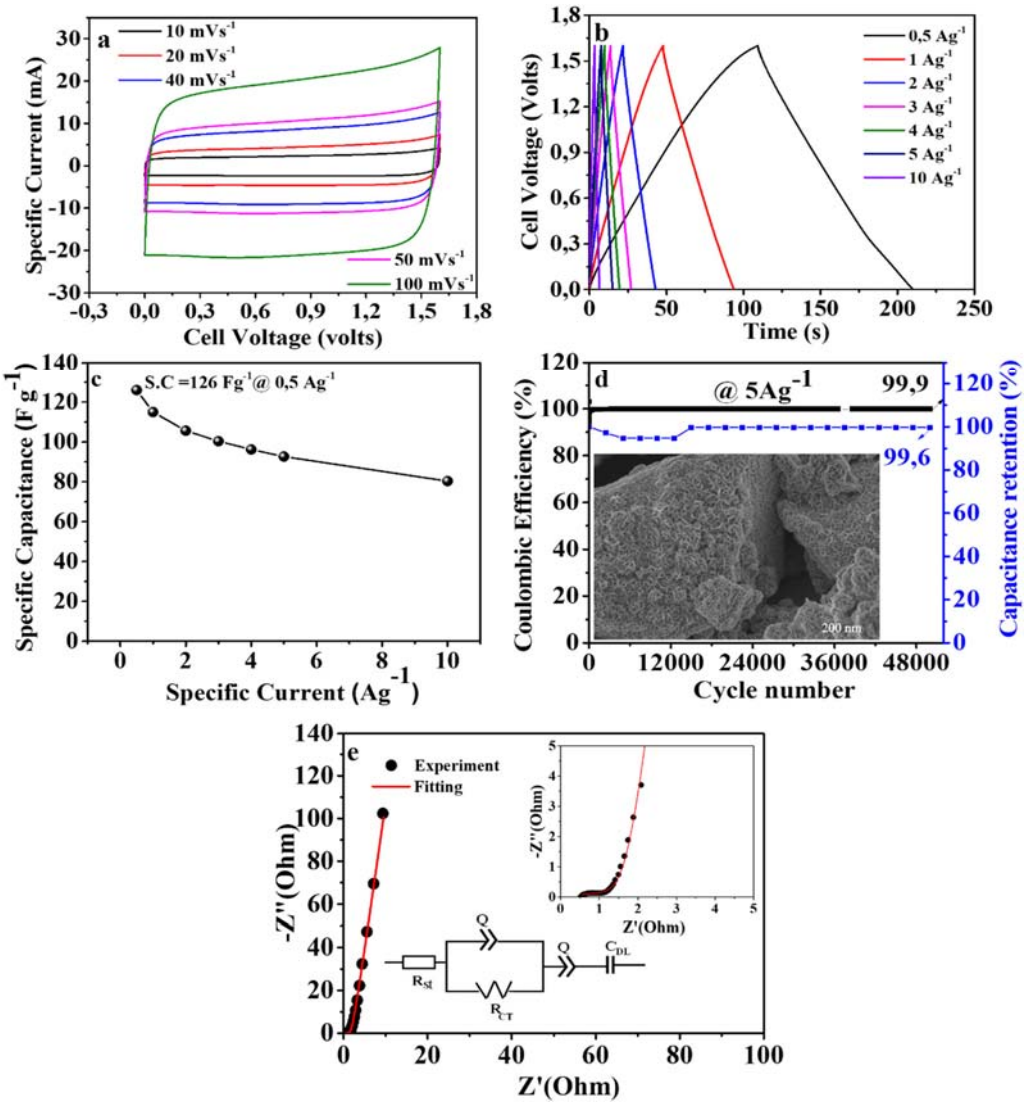

Figure 9: (a) CV curves at different scan rates, (b) GCD curves at different specific currents, (c) specific capacitance versus specific current, (d) capacitance retention and coulombic efficiency against cycle numbers with SEM image as inset after measurement and, (e) fitting of experimental data with equivalent series circuit inset to the figure for (M-S AC//M-S AC) device using 2,5M KNO_3.

Figure S 3 compares the electrochemical characterization before, and after stability. After the stability test, the CV patterns appear to maintain the EDLCs behaviour with a linear quasi-rectangular shape. Similar behaviour can be observed from the GCD patterns as displayed in figure S 3(b). The figure displays triangular GCD patterns with lower discharge time after cycling stability. The device R_s value after stability slightly increase to 0.79 ohms as displayed in figure S 3(c). The device also displays a non-pronounced semi-circle in the low-frequency region after the cycling stability indicating a very small charge transfer resistance between the electrodes and the electrolyte after the test [49]. The EIS features obtained after stability illustrates no major changes as compared to results obtained before stability. This indicates that structure the electrodes material within the device did not experience significant defect through the cycling test.

The device using the aqueous electrolyte yielded insufficient specific energy of 11.5 Wh kg^{-1} at a specific power of 0.4 to $kW \cdot kg^{-1}$. To demonstrate material's capability further, a second symmetric M-S AC//M-S AC device using 1-Ethyl-3-methylimidazolium-bis(fluoroSulfonyl)imide ionic liquid electrolyte (EmiFSI) with a possibility of a wider potential window V was also assembled. A complete three-electrode measurement of the 1:1 K_2CO_3 to M-S AC using EmiFSI was performed, and the results are illustrated in figures S 4 and figure S 5. Despite the non-aqueous electrolyte, the 1:1 K_2CO_3 to M-S AC is seen to illustrate the anticipated EDLC behaviour on its CVs (figure S 4(a) and figure S 4(c)) in both positive and negative potentials. Its GCDs (figure S 4(b) and figure S 4(d)) also illustrated linear triangular shapes. EDLC behaviours are also noticed at various scan rates (figure S 5(a & c)) and distinct specific currents ((figure S 5(b & d)) with sustaining capacitance retention for both positive and negative electrodes measurement (figure S 5(e)). The EIS of the IL/1:1 K_2CO_3 to M-S AC interface in figure S 4(e) displayed an R_s having of 11.6 Ohms. It is

suggested that this high result is also influence by internal resistances within the T-Cell. However, these measurements provided accurate operating parameters to perform a two-electrode analysis using EmiFSI as the electrolyte. Figure 10 displays the device's electrochemical performances when using EmiFSI as the electrolyte. Figure 10(a) displays the CV curves with moderately identical rectangular shapes identical to the CV curves obtained with the aqueous electrolyte (2.5 M KNO_3) in figure 9 (a). Figure 10 (b) illustrates the GCD curves of the ionic liquid device at several specific currents. The GCD curves are symmetric, triangular, and in harmony with the CV curves in figure 10 (a). A specific capacitance of 112.8 F g^{-1} was obtained from the GCD curves at 0.5 A g^{-1}. Figure 10 (c) illustrates the fitting of the Nyquist plot of the EmiFSI device. The circuit also involved a resistor related to the series resistance located at the interface between the electrode and the EmiFSI electrolyte. The leakage resistance (R_L) component presented in the circuit is related to the difficulties of the ions to penetrates the material 'pores due to larger ions size within EmiFSI as compared to KNO_3 [27]. The Nyquist plot of the EmiFSI device displays a light semi-circle and a diffusion path length close to the y-axis as illustrated on figure and inset. An R_s value of 2.3 Ω was recorded for this device. The obtained higher R_s value as compared to the one obtained for the KNO_3 device is expected due to the high conductivity of aqueous electrolytes as highlighted in the literature. As displayed in figure 10 (d), the EmiFSI displays capacitance retention of 80.38 % and coulombic efficiency of 98.1 % after 10000 cycles. This proves the adequate electrochemical stability of the device and its exciting potential as a supercapacitor with a wider potential window despite the decrease in capacitance retention after 5000 cycles which is due material's discreditation due to long cycling. The photograph of the device lighting 4 light emitting diodes (LED) is illustrated in the inset to figure 10 (d). The single device could light the LEDs for ~ 42 seconds which exhibits its usefulness and its practical application prospect.

Figure 10 (e) displays the Ragone plot comparing our device to the similar devices in the literature These values were calculated from the GCD curves at various specific currents. The specific energy (E_s) for the assembled device with 2.5 M KNO_3 varies from 11.19 to 7.13 $Wh \cdot kg^{-1}$, and the specific power (P_s) varies from 8.0 to 0.4 to $kW \cdot kg^{-1}$. The EmiFSI device demonstrated specific energy varying from 28.03 to 5 Wh kg^{-1}, and the specific power varying from 14.0 to 0.7 kW kg^{-1}. The EmiFSI device displayed higher specific energy and power compared to the previously reported mangosteen shell-derived activated carbon materials as shown in the figure [10, 41]. Additionally, the devices also presented higher specific energy and power compared to several other activated carbon from biomass wastes. Table 3 displays a comparison of the specific energy and power of similar plant-based derived activated carbon. The assembled 2.5 M KNO_3 and EmiFSI device have a similar if not higher specific energy and power as compared to the previously reported EDLCs devices. Some of the reported devices using plant-based derived activated carbon doped with heteroatoms demonstrated superior specific energy and power as illustrated in table 3. This indicates hints for future improvement of the as-synthesized 1:1 K_2CO_3 to M-S AC. Overall, the obtained results demonstrated a sustaining reversible adsorption/desorption process of the electrolyte ions during the charge storage occurring within the cell. It also approves the potential of the M-S activated carbon electrode material and the EmiFSI as the electrolyte for high-energy supercapacitors applications.

Table 3: Comparison of the specific energy and power of similar plant-based derived activated carbon.

Precursor	Electrolyte	Specific Capacitance ($F\ g^{-1}$)	Specific Energy ($Wh\ kg^{-1}$)	Specific Power ($W\ kg^{-1}$)	Ref.
Banana peel	$NaNO_3$	165	18.6	485	[24]
Soybean (doped)	KOH/PVA	149.3	10.2	351	[50]
Rose flower	6 M KOH	75.3	15.6	499	[51]
Palm (Doped)	Bmim-TFSI	85	106.3	3000	[52]
Pomelo (Doped)	2 M Li_2SO_4	66.5	36.5	1000	[53]
Capsicum seed	Emim-TFSI	N/A	37	600	[27]
Peanut shell	2.5 M KNO_3	224.3	25.2	900	[5]
Amarula seed husk	2.5 M KNO_3	140	16	450	[29]
Coconut shell	50 % Seawater	186	11	324	[54]
Lignin	2.5 M KNO_3	114	10	397	[55]
Mangosteen shell	6 M KOH	76.8	17.28	401	[10]
Mangosteen shell waste	2.5 M KNO_3	125.9	11.5	400	**This work**
Mangosteen shell waste	**EmiFSI**	**112.8**	28.03	**700**	

A comparison of the performances of the developed device with commercially available capacitors can be seen in Table 4. In terms of the potential window and, capacitance the developed EmiFSI device could compare well with the ones available in the market.

Table 4: EmiFSI-Mangosteen shell waste compared with devices available commercially.

Company	Potential Window (V)	Capacitance (F)	Ref
APowerCap	2.7	450	[56]
Maxwell	2.7	605	
Panasonic	5.50	50	
Yunasko	2.7	510	
EmiFSI -Mangosteen shell waste	**2.8**	**823**	**This work**

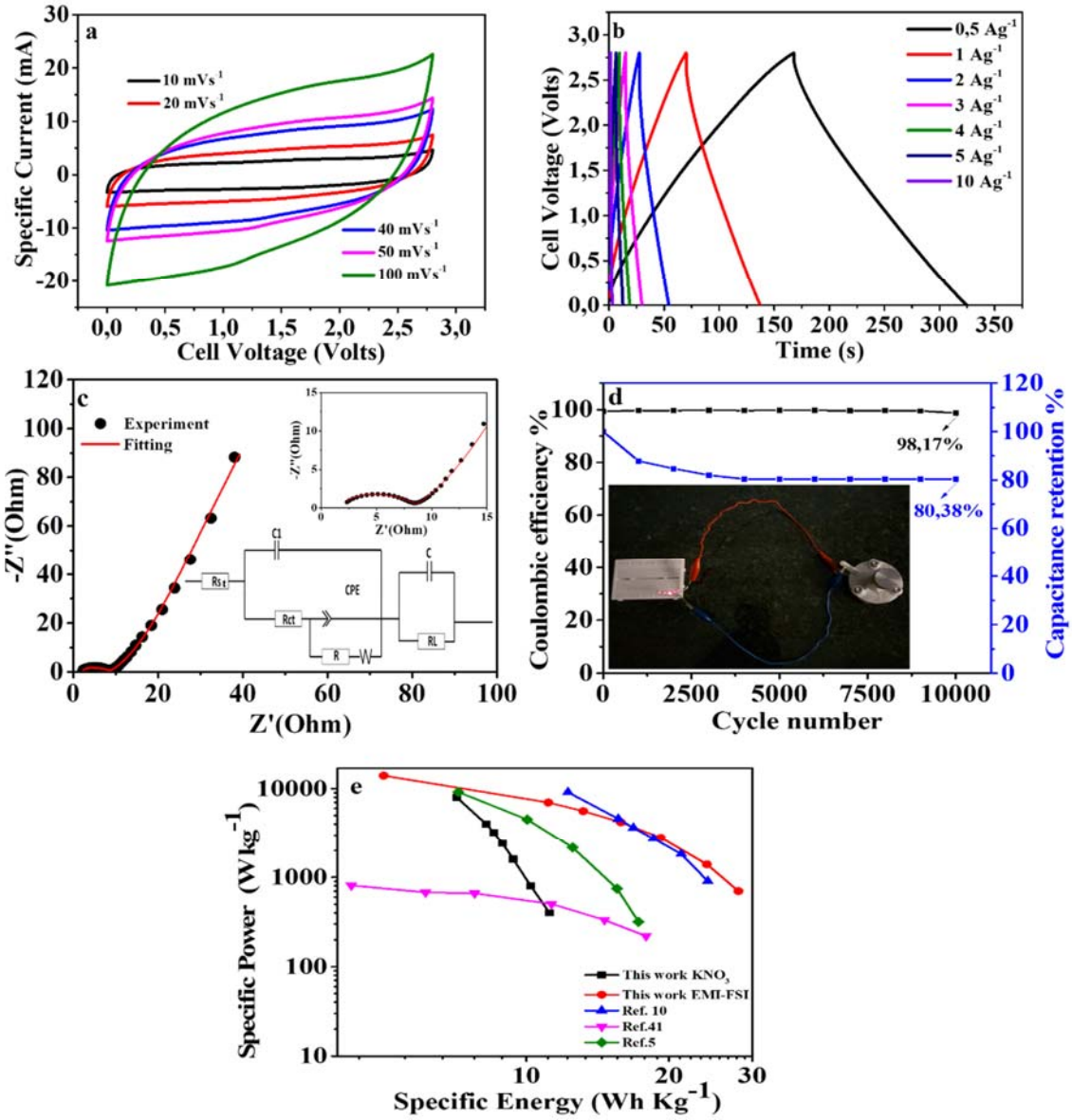

Figure 10: (a) CV curves at different scan rates, (b) GCD curves at different specific currents, (c) fitting of experimental data with equivalent series circuit inset to the figure, (d) capacitance retention and coulombic efficiency against cycle numbers with inset picture of the device lighting 4 light emitting diode for (M-S AC//M-S AC) device using EMI-FSI and (e) Ragone plot.

4. Conclusion

The effect of K_2CO_3, KOH, and H_3PO_4 activating agents and the variation of the K_2CO_3 impregnation ratio on the porosity of M-S AC were successfully investigated. The characterization techniques enabled the determination of the ideal technological parameters for preparing the M-S activated carbon via a one-step merged carbonization/activation process. The optimized porous carbon displayed a high specific surface area of 2802.6 $m^2 g^{-1}$ and a highly ordered mesoporous arrangement. The electrochemical performances of the 1:1 K_2CO_3 to M-S AC via a three-electrode measurement revealed a high specific capacitance of 298.13 F g^{-1} at 0.5 A g^{-1} in a potential window of -0.8 – 0.0 V vs Ag/AgCl using 2.5 M KNO_3 electrolyte. The assembled symmetric supercapacitor using 2.5 M KNO_3 electrolyte demonstrated a specific energy density of 11.5 Wh kg^{-1} at a specific power density of 0.4 kW kg^{-1} and excellent capacitance retention of 99.6 % after 50000 cycles at 20 A g^{-1}. The other assembled symmetric device using EmiFSI in a wider potential window of 2.8 V demonstrated a specific capacitance of 112.8 F g^{-1} at 0.5 A g^{-1} corresponding to a specific energy of 28.03 Wh kg^{-1} at a specific power of 0.7 kW kg^{-1}. The device also proved excellent cycling stability over a cycling test of 10000 charge/discharge cycles conducted at 5 A g^{-1}. The investigation demonstrated the potential use of mangosteen shells as an excellent precursor to produce a high surface area activated carbon at a lower production cost. It also highlighted the benefit of using EmiFSI as the electrolyte for high-energy supercapacitors applications.

5. Acknowledgment

The authors would like to acknowledge the Department of Science and Technology (DST) and the National Research Foundation (NRF) (Grant No. 61056) of South Africa for their financial support for this research. The opinions, observations, and conclusions set out herein are those of the author(s) and the NRF is not liable in this respect in any way. Vianney N. Kitenge also

appreciates financial support from the University of Pretoria and the National Research Foundation for his Ph.D. studies.

6. Declarations

The authors declare that there is no conflict of interest.

7. References.

[1] P. Simon, Y. Gogotsi, Materials for electrochemical capacitors, Nanoscience and Technology: A Collection of Reviews from Nature Journals. (2009) 320–329. https://doi.org/10.1142/9789814287005_0033.

[2] M. Alzaid, F. Alsalh, M.Z. Iqbal, Biomass derived activated carbon-based hybrid supercapacitors, J. Energy Storage. 40 (2021) 102751. https://doi.org/10.1016/J.EST.2021.102751.

[3] A.M. Abioye, F.N. Ani, Recent development in the production of activated carbon electrodes from agricultural waste biomass for supercapacitors: A review, Renewable and Sustainable Energy Reviews. 52 (2015) 1282–1293. https://doi.org/10.1016/J.RSER.2015.07.129.

[4] G. Jiang, R.A. Senthil, Y. Sun, T.R. Kumar, J. Pan, Recent progress on porous carbon and its derivatives from plants as advanced electrode materials for supercapacitors, J. Power Sources. 520 (2022) 230886. https://doi.org/10.1016/J.JPOWSOUR.2021.230886.

[5] N. Sylla, N. Ndiaye, B. Ngom, D.M.-S. reports, undefined 2019, Effect of porosity enhancing agents on the electrochemical performance of high-energy ultracapacitor electrodes derived from peanut shell waste, Nature.Com. (n.d.). https://www.nature.com/articles/s41598-019-50189-x (accessed September 1, 2022).

[6] D. Tarimo, K. Oyedotun, A. Mirghni, N.S.-E., undefined 2020, High energy and excellent stability asymmetric supercapacitor derived from sulphur-reduced graphene oxide/manganese dioxide

composite and activated, Elsevier. (n.d.). https://www.sciencedirect.com/science/article/pii/S0013468620308914 (accessed September 1, 2022).

[7] F. Béguin, V. Presser, A. Balducci, E.F. Frackowiak, E. Frackowiak, V. Presser, A. Balducci, Carbons and Electrolytes for Advanced Supercapacitors, Advanced Materials. 26 (2014) 2219–2251. https://doi.org/10.1002/ADMA.201304137.

[8] G. Yu, X. Xie, L. Pan, Z. Bao, Y. Cui, Hybrid nanostructured materials for high-performance electrochemical capacitors, Nano Energy. 2 (2013) 213–234. https://doi.org/10.1016/J.NANOEN.2012.10.006.

[9] P. Anastas, N. Eghbali, Green Chemistry: Principles and Practice, Chem Soc Rev. 39 (2009) 301–312. https://doi.org/10.1039/B918763B.

[10] V. Yang, R.A. Senthil, J. Pan, A. Khan, S. Osman, L. Wang, W. Jiang, Y. Sun, Highly ordered hierarchical porous carbon derived from biomass waste mangosteen peel as superior cathode material for high performance supercapacitor, Journal of Electroanalytical Chemistry. 855 (2019) 113616. https://doi.org/10.1016/J.JELECHEM.2019.113616.

[11] E. Frackowiak, Carbon materials for supercapacitor application, Physical Chemistry Chemical Physics. 9 (2007) 1774–1785. https://doi.org/10.1039/B618139M.

[12] Y. Wang, A. du Pasquier, D. Li, P. Atanassova, S. Sawrey, M. Oljaca, Electrochemical double layer capacitors containing carbon black additives for improved capacitance and cycle life, Carbon N Y. 133 (2018) 1–5. https://doi.org/10.1016/J.CARBON.2018.03.001.

[13] D. Wang, Z. Xu, Y. Lian, C. Ban, H. Zhang, Nitrogen self-doped porous carbon with layered structure derived from porcine bladders for high-performance supercapacitors, J Colloid Interface Sci. 542 (2019) 400–409. https://doi.org/10.1016/J.JCIS.2019.02.024.

[14] J. Zhang, J. Xue, P. Li, S. Huang, H. Feng, H. Luo, Preparation of metal-organic framework-derived porous carbon and study of its supercapacitive performance, Electrochim Acta. 284 (2018) 328–335. https://doi.org/10.1016/J.ELECTACTA.2018.07.102.

[15] D.J. Tarimo, K.O. Oyedotun, N.F. Sylla, A.A. Mirghni, N.M. Ndiaye, N. Manyala, Waste chicken bone-derived porous carbon materials as high performance electrode for supercapacitor applications, J. Energy Storage. 51 (2022) 104378. https://doi.org/10.1016/J.EST.2022.104378.

[16] M. Xue, C. Chen, Y. Tan, Z. Ren, B. Li, C. Zhang, Mangosteen peel-derived porous carbon: synthesis and its application in the sulphur cathode for lithium sulphur battery, J. Mater Sci. 53 (2018) 11062–11077. https://doi.org/10.1007/S10853-018-2370-9/TABLES/4.

[17] Y. Ding, L. Mo, C. Gao, X. Liu, T. Yu, W. Chen, S. Chen, Z. Li, L. Hu, High-Surface-Area Porous Carbon Flakes Derived from Boat-Fruited Sterculia Seeds for High-Energy-Density Aqueous Symmetric Supercapacitors, ACS Sustain Chem Eng. 6 (2018) 9822–9830. https://doi.org/10.1021/ACSSUSCHEMENG.8B00967/ASSET/IMAGES/LARGE/SC-2018-00967S_0005.JPEG.

[18] H. Quan, X. Fan, W. Wang, W. Gao, Y. Dong, D. Chen, Hierarchically porous carbon derived from biomass: Effect of mesopore and heteroatom-doping on electrochemical performance, Appl. Surf. Sci. 460 (2018) 8–16. https://doi.org/10.1016/J.APSUSC.2018.01.202.

[19] A. Jain, M. Ghosh, M. Krajewski, S. Kurungot, M. Michalska, Biomass-derived activated carbon material from native European deciduous trees as an inexpensive and sustainable energy material for supercapacitor application, J. Energy Storage. 34 (2021) 102178. https://doi.org/10.1016/J.EST.2020.102178.

[20] B. Men, P. Guo, Y. Sun, Y. Tang, Y. Chen, J. Pan, P. Wan, High-performance nitrogen-doped hierarchical porous carbon derived from cauliflower for advanced supercapacitors, J. Mater Sci. 54 (2019) 2446–2457. https://doi.org/10.1007/S10853-018-2979-8/FIGURES/7.

[21] D. Momodu, M. Madito, F. Barzegar, A. Bello, A. Khaleed, O. Olaniyan, J. Dangbegnon, N. Manyala, Activated carbon derived from tree bark biomass with promising material properties for supercapacitors, J. Solid State Electrochemistry. 21 (2017) 859–872. https://doi.org/10.1007/S10008-016-3432-Z/FIGURES/9.

[22] A. Phakkhawan, M. Horprathum, N. Chanlek, H. Nakajima, S. Nijpanich, P. Kumnorkaew, S. Pimanpang, P. Klangtakai, V. Amornkitbamrung, Activated carbons derived from sugarcane bagasse for high-capacitance electrical double layer capacitors, J. of Materials Science: Materials in Electronics. 33 (2022) 663–674. https://doi.org/10.1007/S10854-021-07334-Y/FIGURES/7.

[23] I.S. Ismail, N.A. Rashidi, S. Yusup, Production and characterization of bamboo-based activated carbon through single-step H_3PO_4 activation for CO_2 capture, Environmental Science and Pollution Research. 29 (2022) 12434–12440. https://doi.org/10.1007/S11356-021-15030-X/FIGURES/6.

[24] O. Fasakin, J.K. Dangbegnon, D.Y. Momodu, M.J. Madito, K.O. Oyedotun, M.A. Eleruja, N. Manyala, Synthesis and characterization of porous carbon derived from activated banana peels with hierarchical porosity for improved electrochemical performance, Electrochem. Acta. 262 (2018) 187–196. https://doi.org/10.1016/J.ELECTACTA.2018.01.028.

[25] R. Kayiwa, H. Kasedde, M. Lubwama, J.B. Kirabira, Mesoporous activated carbon yielded from pre-leached cassava peels, Bioresour Bioprocess. 8 (2021) 1–12. https://doi.org/10.1186/S40643-021-00407-0/FIGURES/8.

[26] S. Arun, K.U.V. Kiran, S.M. Kumar, M. Karnan, M. Sathish, S. Mayavan, Effect of orange peel derived activated carbon as a negative additive for lead-acid battery under high-rate discharge condition., J. Energy Storage. 34 (2021) 102225. https://doi.org/10.1016/J.EST.2020.102225.

[27] D. Momodu, N.F. Sylla, B. Mutuma, A. Bello, T. Masikhwa, S. Lindberg, A. Matic, N. Manyala, Stable ionic-liquid-based symmetric supercapacitors from Capsicum seed-porous carbons, Journal of Electroanalytical Chemistry. 838 (2019) 119–128. https://doi.org/10.1016/J.JELECHEM.2019.02.045.

[28] M. Deng, J. Wang, Q. Zhang, Effect of freezing pre-treatment on the performance of activated carbon from coconut shell for supercapacitor application, Mater Lett. 306 (2022) 130934. https://doi.org/10.1016/J.MATLET.2021.130934.

[29] D.J. Tarimo, A.A. Mirghni, K.O. Oyedotun, G. Rutavi, V.N. Kitenge, N. Manyala, Recycling of biomass wastes from amarula husk by a modified facile economical water salt method for high energy density ultracapacitor application, J. Energy Storage. 53 (2022) 105166. https://doi.org/10.1016/J.EST.2022.105166.

[30] J. Cui, W. Hu, Z. Cai, Y. Liu, S. Li, W. Tao, H. Xiang, New medicinal properties of mangosteens: Analgesic activity and pharmacological characterization of active ingredients from the fruit hull of Garcinia mangostana L., Pharmacol Biochem Behav. 95 (2010) 166–172. https://doi.org/10.1016/J.PBB.2009.12.021.

[31] Y. Chen, B. Huang, M. Huang, B. Cai, On the preparation and characterization of activated carbon from mangosteen shell, J. Taiwan Inst Chem Eng. 42 (2011) 837–842. https://doi.org/10.1016/J.JTICE.2011.01.007.

[32] W.Q. Zhang, X. Sui, B. Yu, Y.Q. Shen, H.L. Cong, Preparation of high specific surface area and high adsorptive activated carbon by KOH activation, Https://Doi.Org/10.1080/10584587.2019.1592594. 199 (2019) 22–29.

[33] K.Y. Foo, B.H. Hameed, Factors affecting the carbon yield and adsorption capability of the mangosteen peel activated carbon prepared by microwave assisted K_2CO_3 activation, Chemical Engineering Journal. 180 (2012) 66–74. https://doi.org/10.1016/J.CEJ.2011.11.002.

[34] D. Adinata, W.M.A. Wan Daud, M.K. Aroua, Preparation and characterization of activated carbon from palm shell by chemical activation with K_2CO_3, Bioresour Technol. 98 (2007) 145–149. https://doi.org/10.1016/J.BIORTECH.2005.11.006.

[35] J. Hayashi, T. Horikawa, I. Takeda, K. Muroyama, F. Nasir Ani, Preparing activated carbon from various nutshells by chemical activation with K_2CO_3, Carbon N Y. 40 (2002) 2381–2386. https://doi.org/10.1016/S0008-6223(02)00118-5.

[36] D.T. Bakhoum, K.O. Oyedotun, S. Sarr, N.F. Sylla, V.M. Maphiri, N.M. Ndiaye, B.D. Ngom, N. Manyala, A study of porous carbon structures derived from composite of cross-linked polymers and

reduced graphene oxide for supercapacitor applications, J Energy Storage. 51 (2022) 104476. https://doi.org/10.1016/J.EST.2022.104476.

[37] Y. Li, X. Zhang, R. Yang, G. Li, C. Hu, The role of H_3PO_4 in the preparation of activated carbon from NaOH-treated rice husk residue, RSC Adv. 5 (2015) 32626–32636. https://doi.org/10.1039/C5RA04634C.

[38] M.A. Al-Ghouti, D.A. Da'ana, Guidelines for the use and interpretation of adsorption isotherm models: A review, J. Hazard Mater. 393 (2020) 122383. https://doi.org/10.1016/J.JHAZMAT.2020.122383.

[39] Y. Gao, Q. Yue, B. Gao, A. Li, Insight into activated carbon from different kinds of chemical activating agents: A review, Science of The Total Environment. 746 (2020) 141094. https://doi.org/10.1016/J.SCITOTENV.2020.141094.

[40] Y. Li, X. Wang, M. Cao, Three-dimensional porous carbon frameworks derived from mangosteen peel waste as promising materials for CO2 capture and supercapacitors, Journal of CO_2 Utilization. 27 (2018) 204–216. https://doi.org/10.1016/J.JCOU.2018.07.019.

[41] Y. Iradukunda, G. Wang, X. Li, G. Shi, Y. Hu, F. Luo, K. Yi, A.I.M. Albashir, X. Niu, Z. Wu, High performance of activated carbons prepared from mangosteen (Garcinia mangostana) peels using the hydrothermal process, J. Energy Storage. 39 (2021) 102577. https://doi.org/10.1016/J.EST.2021.102577.

[42] T. Ramesh, N. Rajalakshmi, K.S. Dhathathreyan, L.R.G. Reddy, Hierarchical Porous Carbon Microfibers Derived from Tamarind Seed Coat for High-Energy Supercapacitor Application, ACS Omega. 3 (2018) 12832–12840. https://doi.org/10.1021/ACSOMEGA.8B01850/ASSET/IMAGES/MEDIUM/AO-2018-01850T_M003.GIF.

[43] X.L. Su, S.H. Li, S. Jiang, Z.K. Peng, X.X. Guan, X.C. Zheng, Superior capacitive behaviour of porous activated carbon tubes derived from biomass waste-cotonier strobili fibers, Advanced Powder Technology. 29 (2018) 2097–2107. https://doi.org/10.1016/J.APT.2018.05.018.

[44] A. Bello, N. Manyala, F. Barzegar, A.A. Khaleed, D.Y. Momodu, J.K. Dangbegnon, Renewable pinecone biomass derived carbon materials for supercapacitor application, RSC Adv. 6 (2016) 1800–1809. https://doi.org/10.1039/C5RA21708C.

[45] B. Pal, S. Yang, S. Ramesh, V. Thangadurai, R. Jose, Electrolyte selection for supercapacitive devices: a critical review, Nanoscale Adv. 1 (2019) 3807–3835. https://doi.org/10.1039/C9NA00374F.

[46] V.N. Kitenge, K.O. Oyedotun, O. Fasakin, D.J. Tarimo, N.F. Sylla, X. van Heerden, N. Manyala, Enhancing the electrochemical properties of a nickel–cobalt-manganese ternary hydroxide electrode using graphene foam for supercapacitors applications, Mater. Renew. Sustain. Energy. 10 (2021) 1–16. https://doi.org/10.1007/S40243-021-00192-Y/FIGURES/11.

[47] C. Zhao, Q. Wang, H. Zhang, S. Passerini, X. Qian, Two-Dimensional Titanium Carbide/RGO Composite for High-Performance Supercapacitors, ACS Appl. Mater. Interfaces. 8 (2016) 15661–15667. https://doi.org/10.1021/ACSAMI.6B04767/ASSET/IMAGES/LARGE/AM-2016-04767E_0010.JPEG.

[48] F. Barzegar, A. Bello, D. Momodu, M.J. Madito, J. Dangbegnon, N. Manyala, Preparation and characterization of porous carbon from expanded graphite for high energy density supercapacitor in aqueous electrolyte, J. Power Sources. 309 (2016) 245–253. https://doi.org/10.1016/J.JPOWSOUR.2016.01.097.

[49] K.O. Oyedotun, N. Manyala, Graphene foam–based electrochemical capacitors, Current Opinion Electrochem. 21 (2020) 125–131. https://doi.org/10.1016/J.COELEC.2019.12.010.

[50] M. Chen, D. Yu, X. Zheng, X. Dong, Biomass based N-doped hierarchical porous carbon nanosheets for all-solid-state supercapacitors, J. Energy Storage. 21 (2019) 105–112. https://doi.org/10.1016/J.EST.2018.11.017.

[51] A. Khan, R. Arumugam Senthil, J. Pan, Y. Sun, X. Liu, Hierarchically Porous Biomass Carbon Derived from Natural Withered Rose Flowers as High-Performance Material for Advanced Supercapacitors, Batter Supercaps. 3 (2020) 731–737. https://doi.org/10.1002/BATT.202000046.

[52] S.R. Mangisetti, M. Kamaraj, R. Sundara, Large-scale single-step synthesis of wrinkled N–S doped 3D graphene like nanosheets from Tender palm shoots for high energy density supercapacitors, Int. J. Hydrogen Energy. 46 (2021) 403–415. https://doi.org/10.1016/J.IJHYDENE.2020.09.161.

[53] G. Li, Y. Li, X. Chen, X. Hou, H. Lin, L. Jia, One-step synthesis of N, P co-doped hierarchical porous carbon nanosheets derived from pomelo peel for high performance supercapacitors, J. Colloid Interface Sci. 605 (2022) 71–81. https://doi.org/10.1016/J.JCIS.2021.07.065.

[54] F. Barzegar, A.A. Khaleed, F.U. Ugbo, K.O. Oyeniran, D.Y. Momodu, A. Bello, J.K. Dangbegnon, N. Manyala, Cycling and floating performance of symmetric supercapacitor derived from coconut shell biomass, AIP Adv. 6 (2016) 115306. https://doi.org/10.1063/1.4967348.

[55] B.K. Mutuma, N.F. Sylla, A. Bubu, N.M. Ndiaye, C. Santoro, A. Brilloni, F. Poli, N. Manyala, F. Soavi, Valorization of biodigestor plant waste in electrodes for supercapacitors and microbial fuel cells, Electrochim. Acta. 391 (2021) 138960. https://doi.org/10.1016/J.ELECTACTA.2021.138960.

[56] M. Yassine, D. Fabris, Performance of Commercially Available Supercapacitors, Energies 2017, Vol. 10, Page 1340. 10 (2017) 1340. https://doi.org/10.3390/EN10091340.